




# The magnetic properties of Mn-doped cobalt ferrite films prepared by the spin-coating method

Min Shi<sup>1,\*</sup> , Hao Chen<sup>1</sup>, Shushu Du<sup>1</sup>, Yudong Xu<sup>1</sup>, Ruzhong Zuo<sup>2</sup>, Tiancheng Bai<sup>1</sup>, and Enyang Men<sup>1</sup>

<sup>1</sup> School of Materials Science and Engineering, Hefei University of Technology, Hefei 230069, People's Republic of China

<sup>2</sup> School of Materials Science and Engineering, Anhui Polytechnic University, Wuhu 241005, People's Republic of China

Received: 6 January 2023

Accepted: 26 July 2023

Published online:  
8 August 2023

© The Author(s), under exclusive licence to Springer Science+Business Media, LLC, part of Springer Nature 2023

## ABSTRACT

The films of  $\text{Co}_{1-x}\text{Mn}_x\text{Fe}_2\text{O}_4$  ( $x = 0 - 0.4$ ) were prepared on the substrates of Pt (111)/Ti/SiO<sub>2</sub>/Si by the sol-gel method. The effect of mole fraction of doping Mn ions on the microstructure, ferromagnetism and optic properties was investigated. The results show that, when  $x$  is less than 0.4, Mn ions have dissolved into the crystal lattices of  $\text{CoFe}_2\text{O}_4$  without forming secondary phases. The surfaces of the films of  $\text{Co}_{1-x}\text{Mn}_x\text{Fe}_2\text{O}_4$  possess polygonal and dense structures. The results of Raman show that  $\text{Co}^{2+}$  migrates from octahedral interstice to tetrahedral interstice when  $x$  is greater than 0.2. The results of XPS indicate that, in the  $\text{Co}_{0.8}\text{Mn}_{0.2}\text{Fe}_2\text{O}_4$  film, Fe ions exist in the form of  $\text{Fe}^{2+}$  and  $\text{Fe}^{3+}$  and Mn ions exist in the form of  $\text{Mn}^{2+}$  and  $\text{Mn}^{3+}$ . The results also show that, with increasing mole fraction of Mn ions, the values of saturation magnetization increase firstly, then decrease. When  $x$  is equal to 0.2, there is the maximum value of saturation magnetization ( $443.12 \text{ emu}\cdot\text{cm}^{-3}$ ).

## 1 Introduction

$\text{CoFe}_2\text{O}_4$  materials have been extensively used in magnetic data storage devices, magnetic resonance imaging, sensors, vibrators, and targeted medicine administration [1–4] due to their high saturation magnetization ( $M_s$ ,  $455 \text{ emu}\cdot\text{cm}^{-3}$ ) and good chemical stability [5–8]. The formula of  $\text{CoFe}_2\text{O}_4$  can be expressed as  $(\text{Fe}^{3+})_A[\text{Co}^{2+}\text{Fe}^{3+}]_B\text{O}_4$  or  $(\text{Co}^{2+}\text{Fe}^{3+})_A[\text{Co}^{2+}_{1-\delta}\text{Fe}^{3+}_{1+\delta}]_B\text{O}_4$ , where A represents the tetrahedral interstice and B represents the octahedral interstice.

Researchers have attempted to improve the ferromagnetism, such as the change of annealing temperature [9], oxygen vacancies [10], annealing pressure [11]. Meanwhile some researchers focus on ion doping to  $\text{CoFe}_2\text{O}_4$ , such as  $\text{Cd}^{2+}$ ,  $\text{Zn}^{2+}$ ,  $\text{Al}^{3+}$ . Ghorbani [12] indicated that, substitution of  $\text{Cd}^{2+}$  for  $\text{Co}^{2+}$  helps to increase the saturation magnetization. When the mole fraction of doping  $\text{Cd}^{2+}$  is 0.1, maximum value of saturation magnetization ( $423.6 \text{ emu}\cdot\text{cm}^{-3}$ ) reaches. The results of Andhare show that substitution of  $\text{Zn}^{2+}$  for  $\text{Co}^{2+}$  decreases saturation magnetization [13], which is due to the fact that the replacement of  $\text{Co}^{2+}$  with diamagnetic  $\text{Zn}^{2+}$

Address correspondence to E-mail: mrshimindou@hotmail.com

decreases the magnetic interaction between tetrahedron with octahedron [14, 15]. Some researchers investigated impact of mole fraction of  $\text{Mn}^{2+}$  on ferromagnetism of cobalt ferrites [16, 17]. The results of Henaish [16] show that, with the increase of mole fraction of  $\text{Mn}^{2+}$ , the values of saturation magnetization increase firstly, then decrease. There exists the maximum value of saturation magnetization ( $370.3 \text{ emu}\cdot\text{cm}^{-3}$ ) when  $x = 0.1$ . Nevertheless, Koseoglu [17] found that, with the increase of mole fraction of  $\text{Mn}^{2+}$ , the values of saturation magnetization decrease. In response to above-mentioned results, we re-investigated the impact of mole fraction of doping Mn ions on the ferromagnetism of the films and discussed the impact of variable states of Mn ions on the ferromagnetism of the films.

In this work, Mn ions doped  $\text{CoFe}_2\text{O}_4$  films were prepared by the sol-gel method. Impact of mole fraction of Mn ions on the phase constitution, microstructure and ferromagnetism were investigated. And the relationship between valences of Mn ions in  $\text{Co}_{1-x}\text{Mn}_x\text{Fe}_2\text{O}_4$  films and ferromagnetism were analyzed.

## 2 Experimental

The starting material is cobalt nitrate hexahydrate ( $\text{Co}(\text{NO}_3)_2\cdot 6\text{H}_2\text{O}$ , AR, Sinopharm), iron nitrate hexahydrate ( $\text{Fe}(\text{NO}_3)_3\cdot 9\text{H}_2\text{O}$ , AR, Sinopharm) and manganese acetate tetrahydrate ( $\text{Mn}(\text{CH}_3\text{COO})_2\cdot 4\text{H}_2\text{O}$ , AR, Sinopharm), respectively. A certain amount of cobalt nitrate and manganese acetate were dissolved in acetic acid to form a dark purple solution. Appropriate amount of iron nitrate was dissolved in ethylene glycol methyl ether to obtain another red solution. Then, a certain amount of Polyvinylpyrrolidone was added to a certain amount of ethylene glycol methyl ether to acquire the third solution. The above three solutions were mixed while adding an appropriate amount of N-N dimethylformamide (film-forming agent), heated and stirred for three hours to acquire the precursor solutions of  $\text{Co}_{1-x}\text{Mn}_x\text{Fe}_2\text{O}_4$  ( $x = 0.1, 0.2, 0.3, 0.4$ ). To prepare the films, the above precursor solutions were spin-coated on the substrates of Pt (111)/Ti/SiO<sub>2</sub>/Si at 500 rpm for 15 s and at 6500 rpm for 30 s. Finally, the films were pre-annealed at 400 °C and annealed at 700 °C for 15 min. The above processes were repeated three times to obtain the four-layered films. The detailed

experimental process was shown in Fig. 1. In this work, crystal structure and phase composition were characterized using an X-ray diffractometer (XRD, Philips X'pert PRO MPD). A field emission scanning electron microscope (FE-SEM, SU8020, HITACHI) was used to examine the morphologies of surfaces and cross-sections of films. The phase structure of the films was analyzed by using a confocal laser Raman spectrometer (Raman, HORIBA JOBIN YVON). The ferromagnetism of the films measured by a magnetic measurement system (SQUID-VSM, Quantum Design). Finally, X-ray photoelectron spectroscopy (XPS, ESCALAB250Xi, Thermo) was used to analyze the elements and the valence states in the films.

## 3 Results and discussion

XRD patterns of  $\text{Co}_{1-x}\text{Mn}_x\text{Fe}_2\text{O}_4$  films were shown in Fig. 2. The lattice parameters were listed in Table 1, which indicates the films possess cubic structure. As shown in Fig. 2a, when mole fraction of doping Mn ions is less than 0.4, the peaks from  $\text{Co}_{1-x}\text{Mn}_x\text{Fe}_2\text{O}_4$  films are all composed of those from  $\text{CoFe}_2\text{O}_4$  (JCPDS NO: 22-1086) with cubic spinel structure and Pt (JCPDS NO: 87-0647) with cubic structure on the top layer of the substrates without any peak from impurities. This indicates that Mn ions are dissolved into the lattice of  $\text{CoFe}_2\text{O}_4$  and a substitutional solid solution is formed. However, when mole fraction of doping Mn ions reaches 0.4, the impurity peak from  $\text{Fe}_2\text{O}_3$  appears at 33°. Ounacer [18], Sarker [19] and Velhal [20] also indicated that, in  $\text{CoFe}_2\text{O}_4$ -based films, there existed the impurity peak ( $\text{Fe}_2\text{O}_3$ ) at high concentrations of substitution. It can also be found from Fig. 2b that, with the increase of mole fraction of doping Mn ions, the peak (311) shifts to a smaller value of  $2\theta$  gradually. Meanwhile, from Table 1, it is indicated that, with the increase of mole fraction of doping Mn ions, the lattice parameters increase. This is consistent with the Bragg equation. From the results of XPS which will be discussed, it is found that, although there exist  $\text{Mn}^{2+}$  and  $\text{Mn}^{3+}$  in the  $\text{Co}_{0.8}\text{Mn}_{0.2}\text{Fe}_2\text{O}_4$  film, the main ion for Mn is  $\text{Mn}^{2+}$ . Therefore, the impact of doping of  $\text{Mn}^{2+}$  on lattice parameters will be mainly analyzed. As the ionic radius of  $\text{Mn}^{2+}$  (0.083 nm) is larger than the ionic radius of  $\text{Co}^{2+}$  (0.075 nm), doping of Mn ions will lead to the increase of the lattice parameters and the decrease of  $2\theta$ . Moreover, the grain sizes of the films

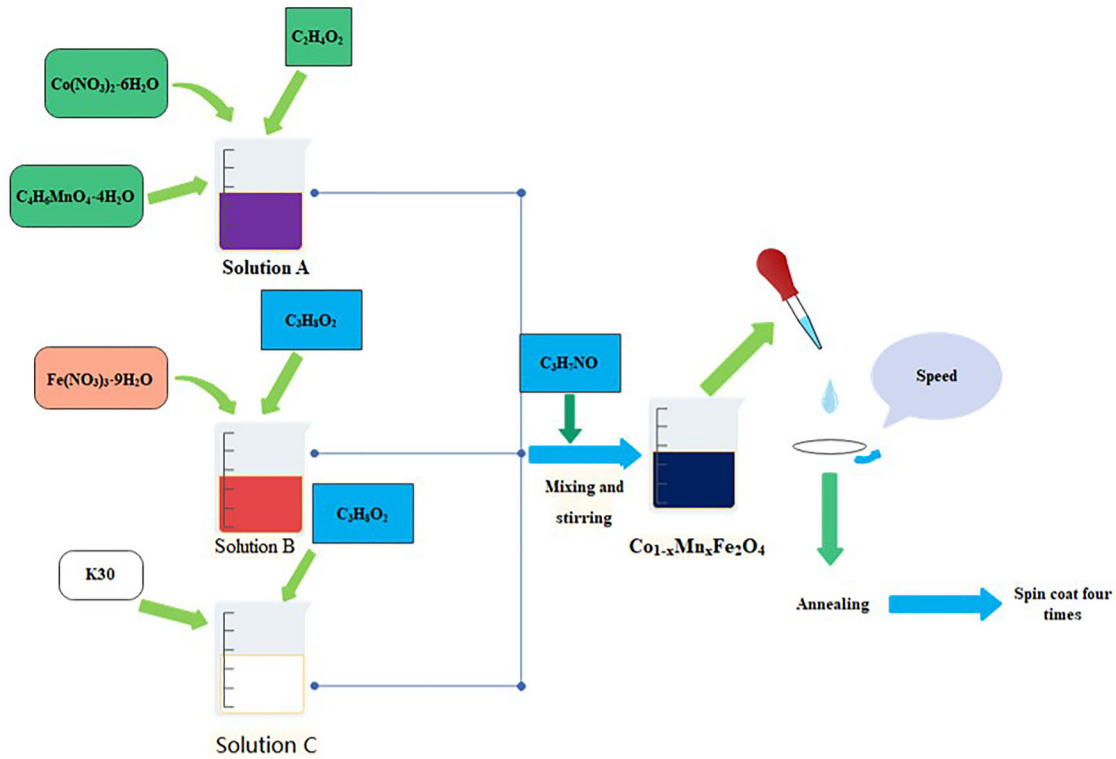
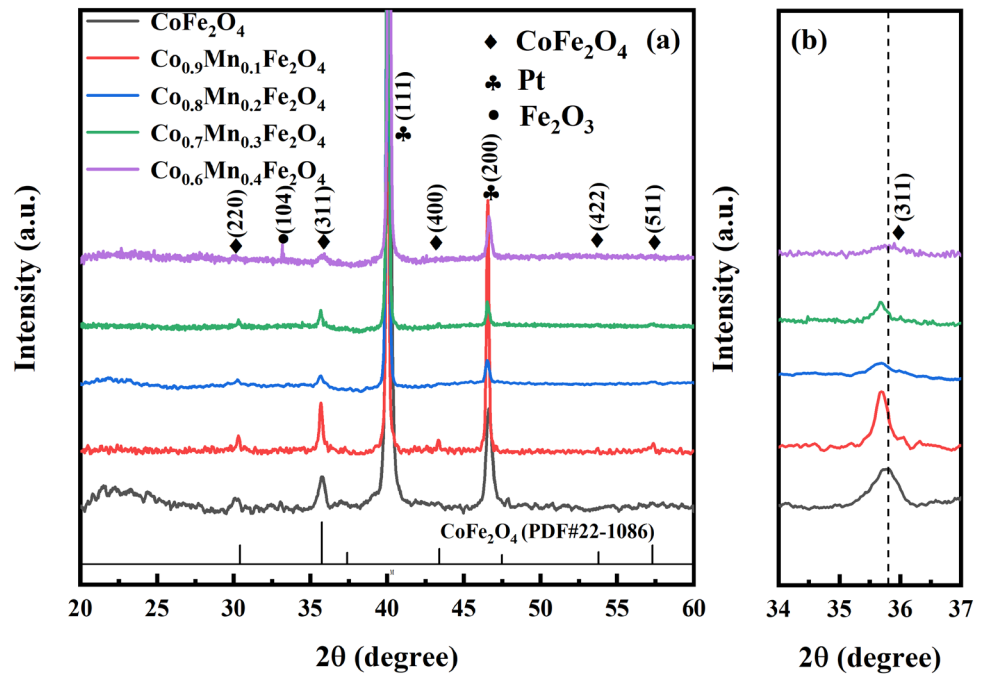


**Fig. 1** Flow chart of preparation process for the films of  $Co_{1-x}Mn_xFe_2O_4$

**Fig. 2 a** XRD patterns of the films of  $Co_{1-x}Mn_xFe_2O_4$  annealed at 700 °C; **b** the enlarged view of diffraction peak at  $\sim 35^\circ$



were calculated through the strongest diffraction peak (311) of the films by using the Scheler equation, as shown in Table 1. It should be noted that the grain sizes of the deposited films decrease with the rise of

mole fraction of doping Mn ions. Ounacer [18] and Imanipour [21] indicated that, with the increase the doping concentration, the solid solution of Mn

**Table 1** Lattice parameters and grain sizes of the films of  $\text{Co}_{1-x}\text{Mn}_x\text{Fe}_2\text{O}_4$  calculated from XRD patterns

Films	Lattice parameters (nm)	a, $\beta$ , $\gamma$	Grain size, D (nm)
$\text{CoFe}_2\text{O}_4$ film	$0.83879 \pm 0.00393$	$90^\circ$	55
$\text{Co}_{0.9}\text{Mn}_{0.1}\text{Fe}_2\text{O}_4$ film	$0.84035 \pm 0.00382$	$90^\circ$	34
$\text{Co}_{0.8}\text{Mn}_{0.2}\text{Fe}_2\text{O}_4$ film	$0.84065 \pm 0.00470$	$90^\circ$	30
$\text{Co}_{0.7}\text{Mn}_{0.3}\text{Fe}_2\text{O}_4$ film	$0.84081 \pm 0.00508$	$90^\circ$	28
$\text{Co}_{0.6}\text{Mn}_{0.4}\text{Fe}_2\text{O}_4$ film	$0.83902 \pm 0.00594$	$90^\circ$	25

ions restricted grain growth and decreased the grain size.

The surface microstructure of the  $\text{Co}_{1-x}\text{Mn}_x\text{Fe}_2\text{O}_4$  films was displayed in Fig. 3. The grain size histograms were also inset in Fig. 3. The results from the histograms were listed in Table 2. As shown in Fig. 3, the surfaces of all films possess polygonal and dense structures. The grain sizes of the  $\text{Co}_{1-x}\text{Mn}_x\text{Fe}_2\text{O}_4$  films estimated from Fig. 3 were also displayed in Table 2. It can be found that, with the rise of mole fraction of doping Mn ions, the grain sizes of the deposited films decrease, which is consistent with the results of XRD. From Table 2, it is seen that size range of grains with the greatest proportion decreases with the increase of mole fraction of doping Mn ions.

The cross-section microstructure of the film of  $\text{Co}_{0.8}\text{Mn}_{0.2}\text{Fe}_2\text{O}_4$  was displayed in Fig. 4. It is seen that there exists a flat upper surface. It can also be found that there is a clear interface and not an intermediate layer between the film and substrate, which implies that no diffusion may exist between the two phases. The film thickness is uniform and the average thickness of the films is about 96 nm.

The Raman spectrum of the  $\text{Co}_{1-x}\text{Mn}_x\text{Fe}_2\text{O}_4$  ( $0 \leq x \leq 0.4$ ) films were shown in Fig. 5. It is known that there are five Raman active modes for the inverse spinel structure, that is  $A_{1g}$ ,  $E_g$  and three  $T_{2g}$  [22]. The wave numbers greater than  $600 \text{ cm}^{-1}$  are related to the vibration of the tetrahedral sublattice in ferrite. And wave numbers which are smaller than  $600 \text{ cm}^{-1}$  are related to the octahedral sublattice [23]. The wave numbers at  $\sim 690$ ,  $\sim 623$ ,  $\sim 564$ ,  $\sim 469$ ,  $\sim 305$  and  $\sim 168 \text{ cm}^{-1}$  belong to the Raman phonon mode of the anti-spinel. When the mole fraction is greater than 0.2, there is a peak at  $\sim 230 \text{ cm}^{-1}$ , indicating the existence of  $\alpha\text{-Fe}_2\text{O}_3$ . As shown in Table 3., the positions of all phonon modes shift

when Co ions were partially replaced by Mn ions, which may be related to the accompanying changes in the cation positions with the increase of mole fraction of Mn ions. Lorentz fitting was performed on all Raman peaks, as shown in Fig. 6. It is observed that, when the mole fraction of Mn ions is less than 0.2, there are only two modes at above  $600 \text{ cm}^{-1}$ . The two modes are related to Fe–O–Fe and Co–O–Fe bonds in the tetrahedral sublattice [24]. Nevertheless, when  $x$  is greater than 0.2, there is the third mode, which corresponds to the transfer of  $\text{Co}^{2+}$  from octahedral to tetrahedral positions, besides the above-mentioned two modes. When doped Mn ions preferentially replace the octahedral interstice occupied by Co ions, the crystal structure will be distorted owing to the different ionic radius of Mn and Co. When the mole fraction of doped Mn ions exceeds 0.2, the crystal structure will be unstable because of excessive distortion. In order to stabilize the crystal structure, part of  $\text{Co}^{2+}$  begins to migrate to the tetrahedral interstice, which is similar to the result of Naik [25] and Lima [26]. UV–Vis spectrum of  $\text{Co}_{1-x}\text{Mn}_x\text{Fe}_2\text{O}_4$  films were shown in Fig. 7a. And the optical band gap ( $E_g$ ) of the film was calculated by the Taucg formula [27].

$$(\alpha h\nu)^2 = B(h\nu - E_g) \quad (1)$$

where  $\alpha$  is the optical absorption coefficient,  $h\nu$  is the photon energy and B is constant, respectively. Relationship of  $(\alpha h\nu)^2$  with  $h\nu$  of the films were shown in Fig. 7b, c, d, e and f. The curves were linear fitted and then  $E_g$  can be acquired from the intersections of linear fitted lines and horizontal axis [27, 28]. Values of  $E_g$  were displayed in Table 4. It is found that, with increasing mole fraction of doping Mn ions, the values of  $E_g$  increase at the beginning, reach the maximum (2.82 eV,  $x = 0.1$ ) and then decrease. The film of

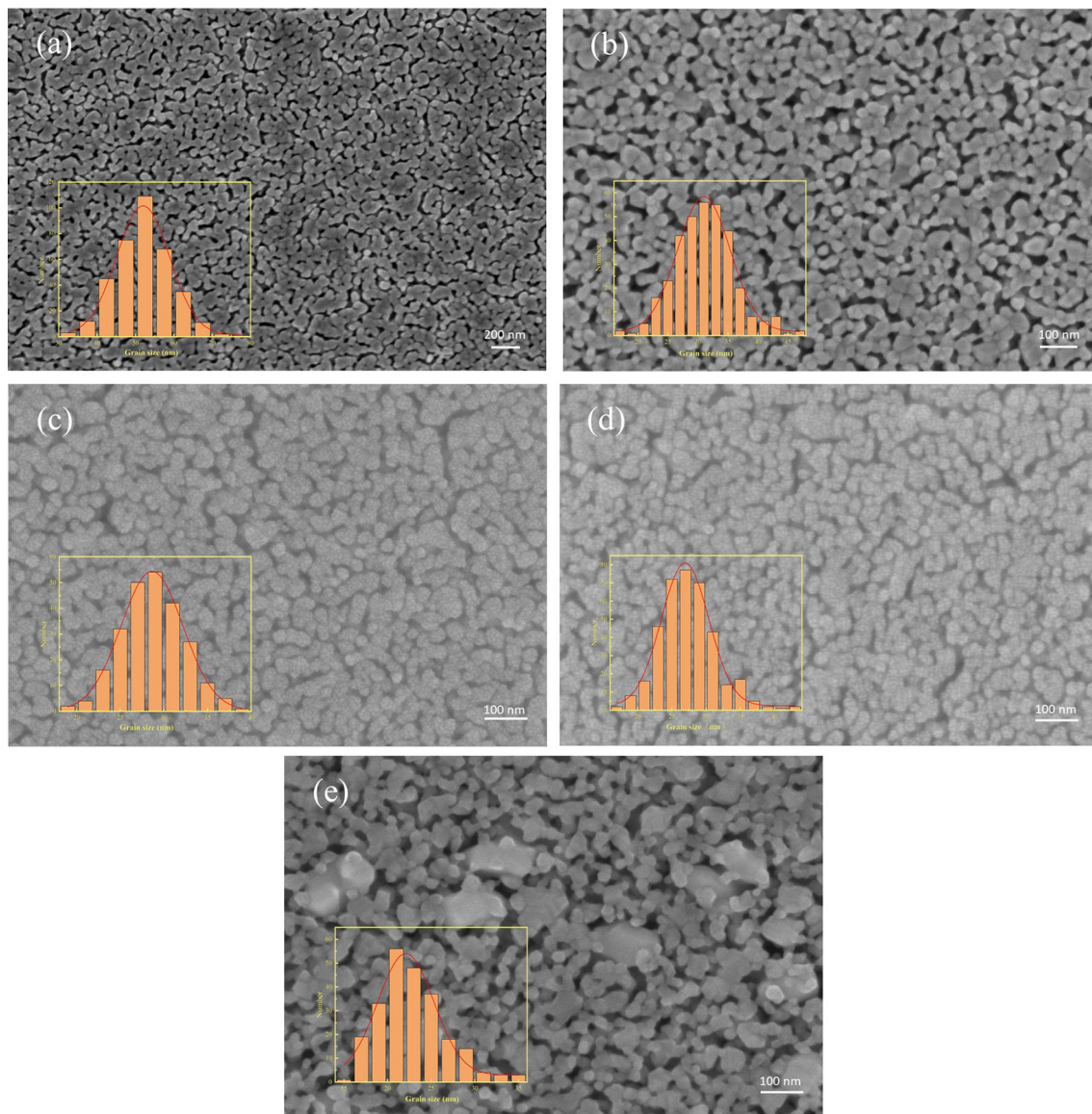


**Fig. 3** FESEM images of the surfaces of the films of  $\text{Co}_{1-x}\text{Mn}_x\text{Fe}_2\text{O}_4$ ; **a**  $x = 0$ ; **b**  $x = 0.1$ ; **c**  $x = 0.2$ ; **d**  $x = 0.3$ ; **e**  $x = 0.4$

**Table 2** Grain size and size range of grains with the greatest proportion obtained from SEM

Films	Grain size, D (nm)	Size range of grains with the highest proportion (nm)
$\text{CoFe}_2\text{O}_4$ film	52.1	50.5–54.5
$\text{Co}_{0.9}\text{Mn}_{0.1}\text{Fe}_2\text{O}_4$ film	31.0	30.2–31.8
$\text{Co}_{0.8}\text{Mn}_{0.2}\text{Fe}_2\text{O}_4$ film	28.6	28.2–29.8
$\text{Co}_{0.7}\text{Mn}_{0.3}\text{Fe}_2\text{O}_4$ film	27.4	26.2–27.8
$\text{Co}_{0.6}\text{Mn}_{0.4}\text{Fe}_2\text{O}_4$ film	22.9	20.2–21.8

$\text{Co}_{0.6}\text{Mn}_{0.4}\text{Fe}_2\text{O}_4$  possesses the minimum value of  $E_g$ , 2.09 eV, which is smaller than that reported in Ref [29]. (2.16 eV). The narrowed band gaps will help to

promote the potential application in light catalytic fields.

The hysteresis loops of the films of  $\text{Co}_{1-x}\text{Mn}_x\text{Fe}_2\text{O}_4$  were displayed in Fig. 8. It is noted that all the curves

**Fig. 4** FESEM image of the cross-section of the film of  $\text{Co}_{0.8}\text{Mn}_{0.2}\text{Fe}_2\text{O}_4$

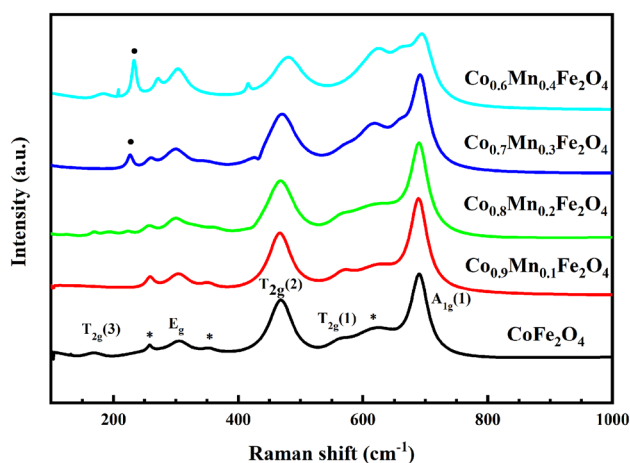
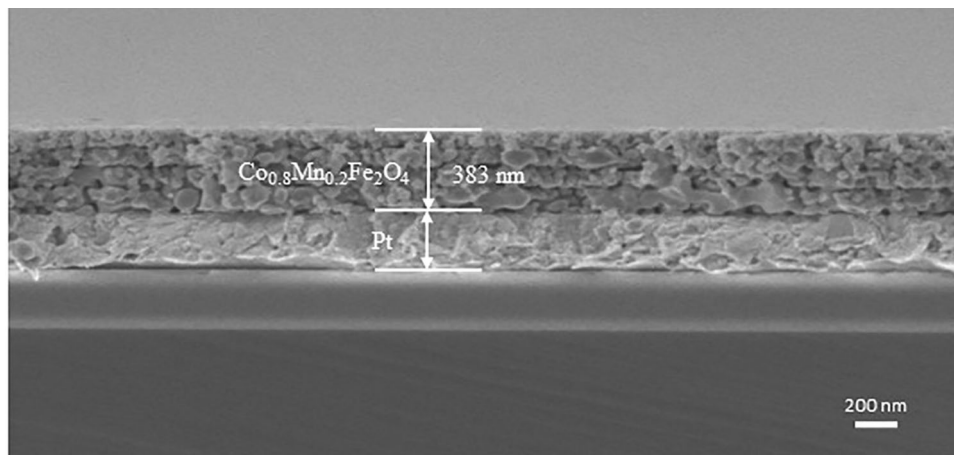


**Fig. 5** The Raman spectra of the films of  $\text{Co}_{1-x}\text{Mn}_x\text{Fe}_2\text{O}_4$

are closed, saturated and symmetric, indicating good ferromagnetism. The magnetic parameters of  $\text{Co}_{1-x}\text{Mn}_x\text{Fe}_2\text{O}_4$  films drawn from Fig. 8 were listed in Table 5. The values of saturation magnetization ( $M_s$ ) of the films increase firstly and then decrease with the increase of  $x$ . When  $x$  is equal to 0.2, there exists the maximum value of saturation magnetization ( $443.12 \text{ emu}\cdot\text{cm}^{-3}$ ), which is greater than those in Table 6 [Ref. 9, 19, 22, 30–32] and close to those in Table 6

**Table 3** The Raman peak positions of the films of  $\text{Co}_{1-x}\text{Mn}_x\text{Fe}_2\text{O}_4$

Doping concentration (x, mol fraction)	$A_{1g}(1)$ ( $\text{cm}^{-1}$ )	$A_{1g}(2)$ ( $\text{cm}^{-1}$ )	$T_{2g}(1)$ ( $\text{cm}^{-1}$ )	$T_{2g}(2)$ ( $\text{cm}^{-1}$ )	*	$E_g$	*	$T_{2g}(3)$ ( $\text{cm}^{-1}$ )
0	690.2	623.0	564.2	468.6	354.0	304.7	258.3	171.2
0.1	690.2	621.3	567.1	465.9	352.3	304.0	258.3	–
0.2	690.2	621.3	566.1	467.6	356.8	300.0	257.2	168.4
0.3	691.9	616.2	571.7	469.4	348.2	299.9	260.7	–
0.4	693.9	619.1	–	480.8	–	302.7	271.5	180.5

\*: Unpredicted anti-spinel Raman peaks

[Ref. 9]. It is known that the values of saturation magnetization increase with the increasing the net magnetic moment,  $M$  [15, 24].  $M$  was calculated from equation (2) [24]:

$$M = |M_B - M_A| \quad (2)$$

where  $M_B$  is the sum of the magnetic moment of all cations at the octahedral interstice and  $M_A$  is the sum of the magnetic moment of all cations at the tetrahedral interstice. From the results of XPS, it is seen that there exists  $\text{Mn}^{2+}$  and  $\text{Mn}^{3+}$  in the  $\text{Co}_{0.8}\text{Mn}_{0.2}\text{Fe}_2\text{O}_4$  film. As the magnetic moment of  $\text{Mn}^{2+}$ ,  $\text{Mn}^{3+}$  and  $\text{Co}^{2+}$  are  $5 \mu_B$ ,  $4 \mu_B$  and  $3 \mu_B$ , respectively. When  $x$  is less than 0.2, with the increase of  $x$ , partial replacement of  $\text{Co}^{2+}$  which occupies the octahedral interstice with  $\text{Mn}^{2+}$  or  $\text{Mn}^{3+}$  will give rise to the increase of  $M_B$ . This leads to the rise of  $M$  [12, 14] and the corresponding rise of the values of saturation magnetization. Nevertheless, when  $x$  is greater than 0.2, the decrease of saturation magnetization can be attributed to the following two reasons. Firstly, the transfer of  $\text{Co}^{2+}$  from the octahedral interstice to the tetrahedral interstice leads to the increase of  $M_A$  and the decrease of  $M_B$ , which gives rise to the decrease of  $M$ . This leads to the decrease of the values of

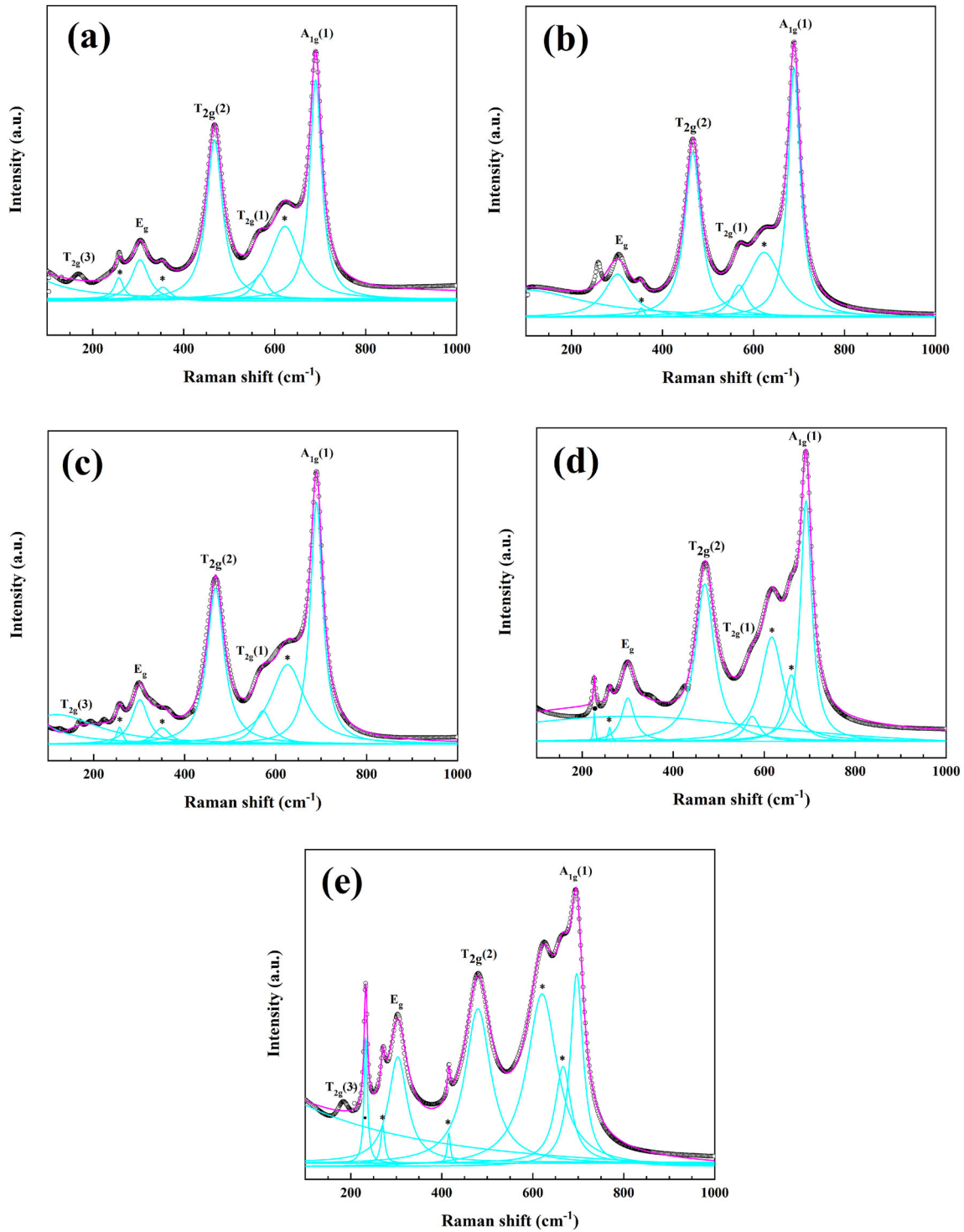


**Fig. 6** The Raman spectrum deconvolution of the films of  $\text{Co}_{1-x}\text{Mn}_x\text{Fe}_2\text{O}_4$ ; **a**  $x = 0$ ; **b**  $x = 0.1$ ; **c**  $x = 0.2$ ; **d**  $x = 0.3$ ; **e**  $x = 0.4$

saturation magnetization. Secondly, the existence of paramagnetic  $\text{Fe}_2\text{O}_3$  will also decrease the values of saturation magnetization.

As shown in Table 5, the values of coercivity ( $H_c$ ) increase firstly, then decrease. When  $x$  is equal to 0.1,

there is the maximum of coercivity (2097 Oe). It is reported that, when the average grain size is greater than 30 nm, there exists multi-domain structure. And the values of coercive force increase with the decrease of grain sizes [22, 33]. However, when the average

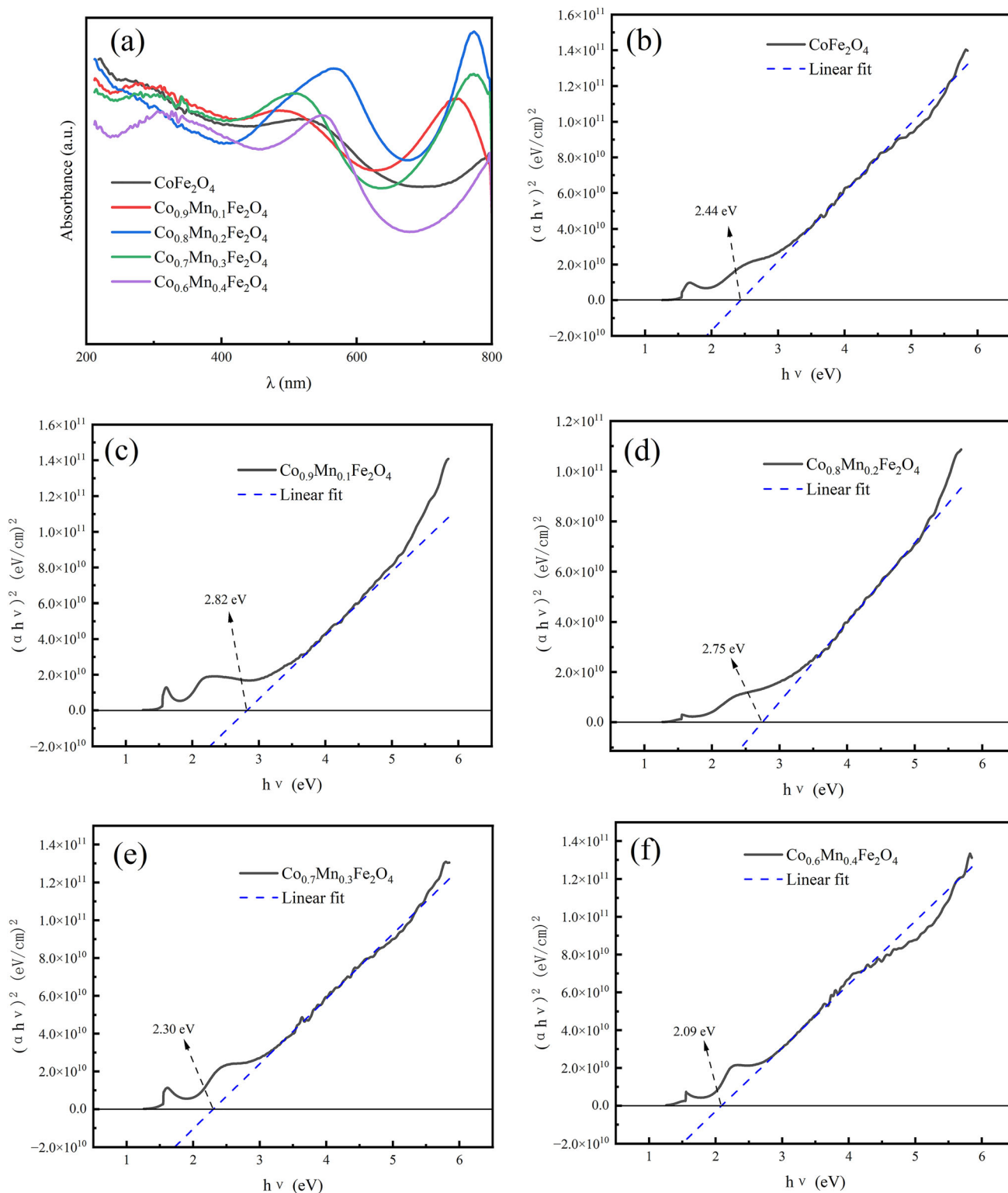


**Fig. 7** Absorbance spectra and Band gap of the films of  $\text{Co}_{1-x}\text{Mn}_x\text{Fe}_2\text{O}_4$ ; **a** Absorbance spectra; **b** Band gap of  $\text{CoFe}_2\text{O}_4$  film; **c** Band gap of  $\text{Co}_{0.9}\text{Mn}_{0.1}\text{Fe}_2\text{O}_4$  film; **d** Band gap

of  $\text{Co}_{0.8}\text{Mn}_{0.2}\text{Fe}_2\text{O}_4$  film; **e** Band gap of  $\text{Co}_{0.7}\text{Mn}_{0.3}\text{Fe}_2\text{O}_4$  film; **f** Band gap of  $\text{Co}_{0.6}\text{Mn}_{0.4}\text{Fe}_2\text{O}_4$  film



**Table 4** Band gap of the films of  $\text{Co}_{1-x}\text{Mn}_x\text{Fe}_2\text{O}_4$

Films	Band gap (eV)
$\text{CoFe}_2\text{O}_4$ film	2.44
$\text{Co}_{0.9}\text{Mn}_{0.1}\text{Fe}_2\text{O}_4$ film	2.82
$\text{Co}_{0.8}\text{Mn}_{0.2}\text{Fe}_2\text{O}_4$ film	2.75
$\text{Co}_{0.7}\text{Mn}_{0.3}\text{Fe}_2\text{O}_4$ film	2.30
$\text{Co}_{0.6}\text{Mn}_{0.4}\text{Fe}_2\text{O}_4$ film	2.09

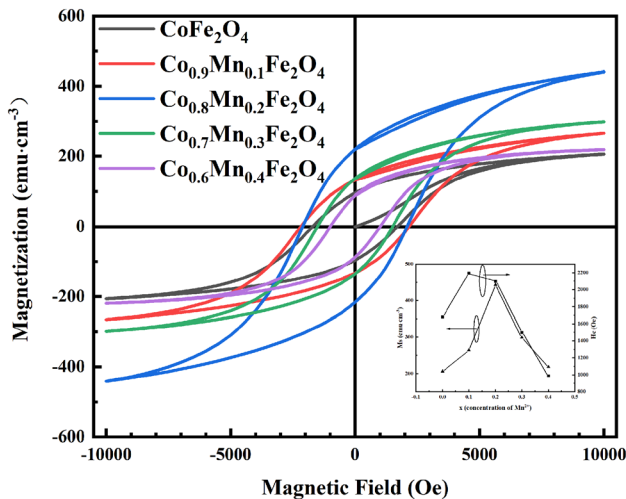


**Fig. 8** The hysteresis loops of the films of  $\text{Co}_{1-x}\text{Mn}_x\text{Fe}_2\text{O}_4$

**Table 5** The magnetic parameters of the films of  $\text{Co}_{1-x}\text{Mn}_x\text{Fe}_2\text{O}_4$

Doping concentration (x, mol fraction)	$M_s$ ( $\text{emu}\cdot\text{cm}^{-3}$ )	$M_r$ ( $\text{emu}\cdot\text{cm}^{-3}$ )	$H_c$ (Oe)
0	206.45	95.76	1680.57
0.1	264.18	129.37	2192.89
0.2	443.12	220.03	2097.13
0.3	298.81	135.48	1498.63
0.4	218.34	87.61	986.32

**Table 6** The values of  $M_s$  from the results of other researchers

Synthesis technology	Doped element	Maximum of $M_s$ ( $\text{emu}\cdot\text{cm}^{-3}$ )	References
chemical solution approach	–	438.2 ( $\text{CoFe}_2\text{O}_4$ )	[9]
sol–gel method	Sn/Fe	282.4 ( $\text{CoFe}_{1.8}\text{Sn}_{0.2}\text{O}_4$ )	[19]
sol–gel method	Mg/Co	336.1 ( $\text{Co}_{0.8}\text{Mg}_{0.2}\text{Fe}_2\text{O}_4$ )	[22]
sol–gel route	Zn/Co	175.2 ( $\text{Co}_{0.8}\text{Zn}_{0.2}\text{Fe}_2\text{O}_4$ )	[30]
sol–gel technique	–	276.1 ( $\text{CoFe}_2\text{O}_4$ )	[31]
sol–gel auto-combustion method	Zn/Co	360.9 ( $\text{Co}_{0.8}\text{Zn}_{0.2}\text{Fe}_2\text{O}_4$ )	[32]

grain size is greater than 30 nm, there exists single-domain structure. And the values of coercive force decrease with the decrease of grain sizes [33–35]. As shown in Table 2, when  $x$  is less than or equal to 0.1, the average grain sizes are greater than 30 nm. This can explain the increase of the values of coercivity ( $H_c$ ) at the beginning. Nevertheless, when  $x$  is greater than 0.1, the average grain sizes are smaller than 30 nm. This gives the reason for the decrease of the values of coercivity ( $H_c$ ) with the further increase of  $x$ .

XPS spectra of the film of  $\text{Co}_{0.8}\text{Mn}_{0.2}\text{Fe}_2\text{O}_4$  was displayed in Fig. 9. As shown in Fig. 9a, there are peaks from Co 2p, Fe 2p, Mn 2p, O 1s, and C 1s. Binding energy values for all elements were corrected by the C1s standard peak at 284.8 eV. From Fig. 9b, it is seen that the binding energies at 786.95 and 803.05 eV are related with the oscillatory satellite peaks of Co 2p<sub>3/2</sub> and Co 2p<sub>1/2</sub>, respectively. The peaks from Co 2p<sub>3/2</sub> can be divided into 780.4 and 782.05 eV by deconvolution, which means the existence of  $\text{Co}^{2+}$ . It can also be seen that there exists Co 2p<sub>1/2</sub> deconvolution located at 796.35 eV, which may be attributed to the existence of  $\text{Co}^{3+}$  [36]. It is clear that the satellite peak of  $\text{Co}^{2+}$  is much higher than that of  $\text{Co}^{3+}$ . This may be due to the unpaired valence electrons in  $\text{Co}^{3+}$ , which makes the spin state lower than that of  $\text{Co}^{2+}$ . The binding energy of Fe were shown in Fig. 9c. It is seen that there are two peaks at 718.35 and 733.45 eV, which are the oscillating satellite peaks from Fe 2p<sub>3/2</sub> and Fe 2p<sub>1/2</sub>, respectively. The peaks from Fe 2p<sub>3/2</sub> can be divided into two peaks at 710.68 and 712.75 eV, which belong to those of  $\text{Fe}^{3+}$ . The lower binding energy means that  $\text{Fe}^{3+}$  occupies the octahedral site, while the higher binding energy indicates  $\text{Fe}^{3+}$  occupies the tetrahedral site [37]. The peak at 724.85 eV indicates the existence of  $\text{Fe}^{2+}$ . Compared with the main peak,

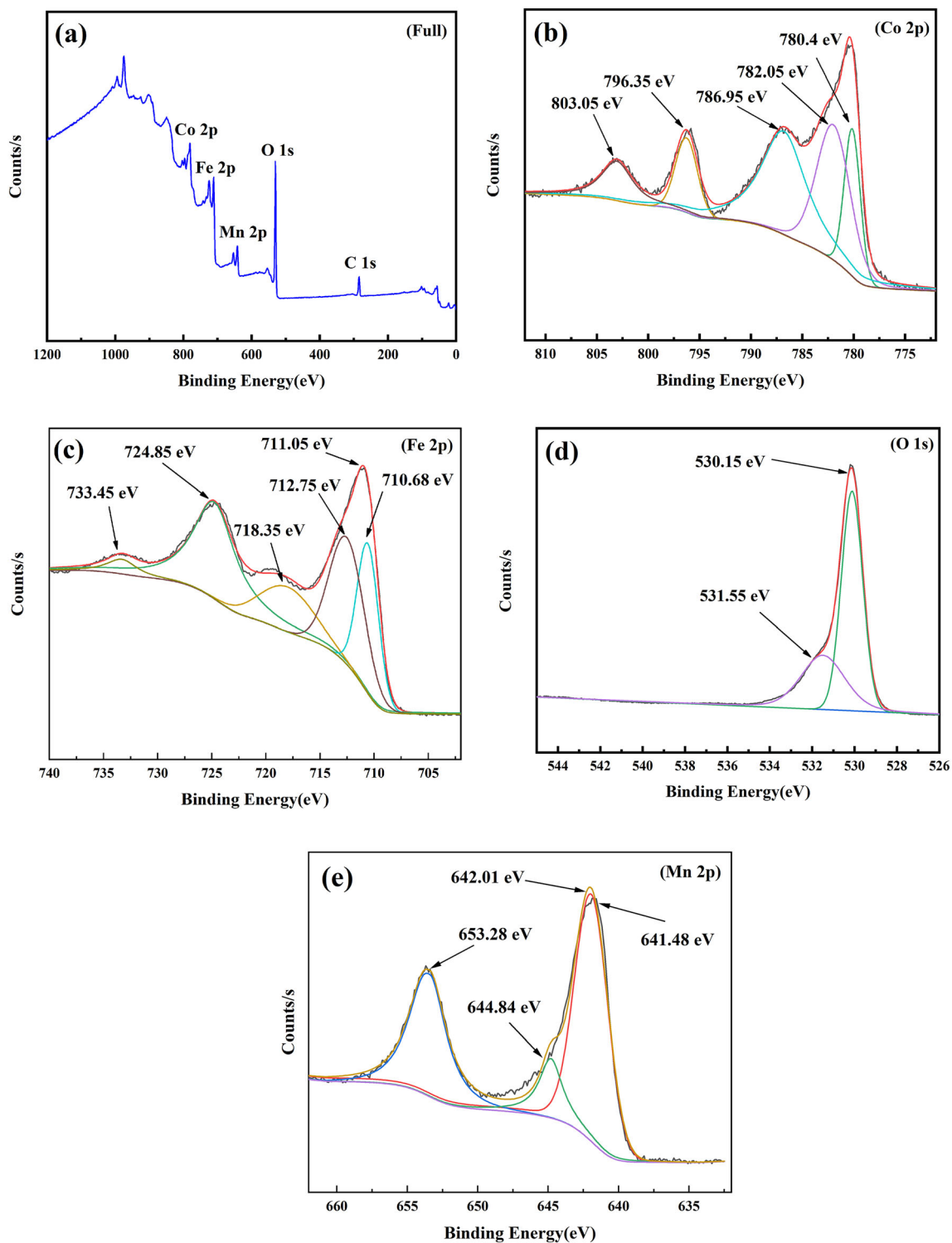


**Fig. 9** XPS spectrum of the film of  $\text{Co}_{0.8}\text{Mn}_{0.2}\text{Fe}_2\text{O}_4$ ; **a** full spectrum; **b** the enlarged view of Co2p; **c** the enlarged view of Fe2p; **d** the enlarged view of O1s; **e** the enlarged view of Mn2p

the oscillating peaks are not obvious, implying that  $\text{Fe}^{3+}$  is the main form of Fe ions. The peaks from O 1s can be deconvoluted into two peaks at 530.15 and

531.55 eV, as demonstrated in Fig. 9d. The peak at 531.55 eV is related with  $\text{H}_2\text{O}$  adsorbed on the surfaces of the films. And the peak at 530.15 eV

**Table 7** Ionic radii and Percentage of difference of ionic radii

Ions	Ionic radii (nm)	Percentage of difference of ionic radii (%)
Mn <sup>2+</sup>	0.083	10.67 ( $(\frac{r_{Mn^{2+}} - r_{Co^{2+}}}{r_{Co^{2+}}})$ )
Mn <sup>3+</sup>	0.065	13.33 ( $(\frac{r_{Mn^{3+}} - r_{Co^{2+}}}{r_{Co^{2+}}})$ )
Mn <sup>4+</sup>	0.053	29.33 ( $(\frac{r_{Mn^{4+}} - r_{Co^{2+}}}{r_{Co^{2+}}})$ )
Co <sup>2+</sup>	0.075	–

corresponds to O<sup>2-</sup>. Figure 9e showed the spectral peaks of Mn 2p in Co<sub>0.8</sub>Mn<sub>0.2</sub>Fe<sub>2</sub>O<sub>4</sub>. The main peak at 641.48 eV is related to Mn 2p<sub>3/2</sub>, while 653.28 eV corresponds to the spectral peak of Mn 2p<sub>1/2</sub>. And the peak from Mn 2p<sub>3/2</sub> is divided into two peaks at 642.01, 644.84 eV by deconvolution. The lower binding energy represents Mn<sup>2+</sup>, while the higher binding energy represents Mn<sup>3+</sup> [38]. By deconvolution, it can be obtained that the atomic ratio of Mn<sup>2+</sup> to Mn<sup>3+</sup> is about 4.6:1. Therefore, in the film, the main ion for Mn is Mn<sup>2+</sup> not Mn<sup>3+</sup>. Considering Mn ions partially replace Co<sup>2+</sup> to form substitutional solid solutions, when the radii of Mn ions are close to those of Co<sup>2+</sup>, the lattice distortion will be reduced which makes substitutional solid solution more stable. We have calculated the percentage difference of ion radii between the ionic radii of Mn<sup>2+</sup>, Mn<sup>3+</sup> and Mn<sup>4+</sup> with Co<sup>2+</sup> respectively. The results were listed in Table 7. As shown in Table 7, among Mn<sup>2+</sup>, Mn<sup>3+</sup> and Mn<sup>4+</sup>, the ionic radius of Mn<sup>2+</sup> is closest to Co<sup>2+</sup>, so Mn<sup>2+</sup> is easiest to occupy the position of Co<sup>2+</sup> to form substitutional solid solution.

## 4 Conclusions

The films of Co<sub>1-x</sub>Mn<sub>x</sub>Fe<sub>2</sub>O<sub>4</sub> were prepared by the sol-gel method. The results show that the crystal constants decrease with increasing mole fraction of Mn ions. And there exist clear interfaces between the films and the substrates. The results also indicate that the positions of all phonon modes shift when doped with Mn ions. With increasing the mole fraction of Mn ions, the values of the saturation magnetization increase firstly, reach maximum, then decrease. When the mole fraction of Mn ions is equal to 0.2, there exists the maximum saturation magnetization, 443.12 emu·cm<sup>-3</sup>.

## Acknowledgements

The authors acknowledge the financial support from Joint Fund of National Natural Science Foundation of China (U19A2087).

## Author contributions

MS designed the work, revised the manuscript in detail, and approved the final version of the manuscript. HC performed all the experimental work, collected and analyzed the data, and wrote the first draft of the manuscript. SD revised the manuscript and approved the final version of the manuscript.

## Funding

This study was supported by National Natural Science Foundation of China [Grant No. U19A2087].

## Data availability

The authors confirm that the data supporting the findings of this study are available within the article.

## Declarations

**Conflict of interest** The authors declare that they have no known competing financial interests or personal relationships that could have appeared to influence the work reported in this paper.

**Ethical approval** The authors formally declare that the present paper is complied with ethical standards.

## References

- Z. Liu, L.J. Deng, B. Peng, Ferromagnetic and ferroelectric two-dimensional materials for memory application. *Nano Res.* **14**, 1802–1813 (2021)
- S.B. Narang, K. Pubby, Nickel spinel ferrites: a review. *J. Magn. Magn. Mater* **519**, 167163 (2021)
- R. Ranga, A. Kumar, P. Kumari, P. Singh, V. Madaan, K. Kumar, Ferrite application as an electrochemical sensor: a review. *Mater. Charact.* **178**, 111269 (2021)
- O.K. Mmeseles, N. Masunga, A. Kuvarega, T.T. Nkambule, B.B. Mamba, K.K. Kefeni, Cobalt ferrite nanoparticles and nanocomposites: Photocatalytic, antimicrobial activity and toxicity in water treatment. *Mat. Sci. Semicon. Proc.* **123**(2020)
- M. Kishimoto, E. Kita, H. Yanagihara, Effect of lattice mismatch on magnetic properties of acicular spinel iron oxide particles with crystallized cobalt ferrite layer. *J. Magn. Magn. Mater.* **510**, 166932 (2020)
- C.M. Magdalane, G.M.A. Priyadharsini, K. Kaviyarasu, A.I. Jothi, G.G. Simiyon, Synthesis and characterization of TiO<sub>2</sub> doped cobalt ferrite nanoparticles via microwave method: investigation of photocatalytic performance of congo red degradation dye. *Surf. Interfac.* **25**, 101296 (2021)
- T.E.P. Alves, H.V.S. Pessoni, A. Franco, C. Burda, A.C.S. Samiam, Magnetic-plasmonic properties of CoFe<sub>2</sub>O<sub>4</sub>@Au nanocomposite. *J. Phys. Chem. Solids.* **164**, 110630 (2022)
- H.D.T. Duong, D.T. Nguyen, K.S. Kim, Effects of process variables on properties of CoFe<sub>2</sub>O<sub>4</sub> nanoparticles prepared by solvothermal process. *Nanomaterials* **11**, 3056 (2021)
- R. Illa, R. Jesko, R. Silber, O. Zivotsky, K.M. Kutlakova, L. Matejova, M. Kolencik, J. Pistora, J. Hamrle, Structural, magnetic, optical, and magneto-optical properties of CoFe<sub>2</sub>O<sub>4</sub> thin films fabricated by a chemical approach. *Mater. Res. Bull.* **117**, 96–102 (2019)
- D. Lee, C.W. Cho, J.W. Kim, J.S. Bae, H.J. Yun, J. Lee, S. Park, Effect of oxygen vacancies in the magnetic properties of the amorphous CoFe<sub>2</sub>O<sub>4</sub> films. *J. Non-Cryst. Solids* **456**, 83–87 (2017)
- S.Y. Huang, C.W. Chong, P.H. Chen, H.L. Li, M.K. Li, J.C.A. Huang, Annealing pressure induced ions transfer in Cobalt-Ferrite thin films on amorphous SiO<sub>2</sub>/Si substrates. *J. Magn. Magn. Mater.* **441**, 537–541 (2017)
- H. Ghorbani, M. Eshraghi, A.A.S. Dodaran, Structural and magnetic properties of cobalt ferrite nanoparticles doped with cadmium. *Phys. B* **634**, 413816 (2022)
- D.D. Andhare, S.R. Patade, J.S. Kounsalye, K.M. Jadhav, Effect of Zn doping on structural, magnetic and optical properties of cobalt ferrite nanoparticles synthesized via. Co-precipitation method. *Phys. B* **583**, 412051 (2020)
- Q. Lin, Y. He, J.M. Xu, J.P. Lin, Z.P. Guo, F. Yang, Effects of Al<sup>3+</sup> substitution on structural and magnetic behavior of CoFe<sub>2</sub>O<sub>4</sub> Ferrite Nanomaterials. *Nanomaterials* **8**, 750 (2018)
- G.P. Nethala, R. Tadi, G.R. Gajula, P.V.P. Madduri, A.V. Anupama, V. Veeraiah, Influence of cr on structural, spectroscopic and magnetic properties of CoFe<sub>2</sub>O<sub>4</sub> grown by the wet chemical method. *Mater. Chem. Phys.* **238**, 121903 (2019)
- A.M.A. Henaish, O.M. Hemeda, A. Alqarni, D.E. El Refaay, S. Mohamed, M.A. Hamad, The role of flash auto-combustion method and mn doping in improving dielectric and magnetic properties of CoFe<sub>2</sub>O<sub>4</sub>. *Appl. Phys. A-Mater.* **126**, 834 (2020)
- Y. Koseoglu, F. Alan, M. Tan, R. Yilgin, M. Ozturk, Low temperature hydrothermal synthesis and characterization of Mn doped cobalt ferrite nanoparticles. *Ceram. Int.* **38**, 3625–3634 (2012)
- M. Ounacer, A. Essoumhi, M. Sajieddine, A. Razouk, A. Fnidiki, F. Richomme, J. Juraszek, S.M. Dubiel, M. Sahlaoui, Substitutional effect of Mg<sup>2+</sup> on structural and magnetic properties of cobalt nanoferrite. *J. Phys. Chem. Solids.* **148**, 109687 (2021)
- M.S.I. Sarker, A. Kumar, M.M. Haque, M.M. Rahman, M.K.R. Khan, Structural, morphological and magnetic properties of Sn doped CoFe<sub>2</sub>O<sub>4</sub> nanoparticles. *J. Magn. Magn. Mater.* **541**, 168542 (2021)
- N.B. Velhal, N.D. Patil, A.R. Shelke, N.G. Deshpande, V.R. Puri, Structural, dielectric and magnetic properties of nickel substituted cobalt ferrite nanoparticles: Effect of nickel concentration. *Aip Adv.* **5**, 097166 (2015)
- P. Imanipour, S. Hasani, M. Afshari, S. Sheykh, A. Seifodini, K. Jahanbani-Ardakani, The effect of divalent ions of zinc and strontium substitution on the structural and magnetic properties on the cobalt site in cobalt ferrite. *J. Magn. Magn. Mater.* **510**, 166941 (2020)
- H. Ghorbani, M. Eshraghi, A.A.S. Dodaran, P. Kameli, S. Protasowicki, C. Johnson, D. Vashae, Effect of Yb doping on the structural and magnetic properties of cobalt ferrite nanoparticles. *Mater. Res. Bull.* **147**, 111642 (2022)
- R. Tursun, Y.C. Su, J. Zhang, R. Yakefu, Structural, magnetic, and microwave absorbing properties of NiTiO<sub>3</sub>/CoFe<sub>2</sub>O<sub>4</sub> composites. *J. Alloy Compd.* **911**, 165051 (2022)
- I.H. Dunn, S.E. Jacobo, P.G. Bercoff, Structural and magnetic influence of yttrium-for-iron substitution in cobalt ferrite. *J. Alloy Compd.* **691**, 130–137 (2017)
- S.R. Naik, A.V. Salker, Change in the magnetostructural properties of rare earth doped cobalt ferrites relative to the magnetic anisotropy. *J. Mater. Chem.* **22**, 2740–2750 (2012)
- A.C. Lima, A.P.S. Peres, J.H. Araujo, M.A. Morales, S.N. Medeiros, J.M. Soares, D.M.A. Melo, A.S. Carrico, The

- effect of  $\text{Sr}^{2+}$  on the structure and magnetic properties of nanocrystalline cobalt ferrite. *Mater. Lett.* **145**, 56–58 (2015)
27. J. Revathi, M.J. Abel, V. Archana, T. Sumithra, R. Thiruneelakandan, Synthesis and characterization of  $\text{CoFe}_2\text{O}_4$  and Ni-doped  $\text{CoFe}_2\text{O}_4$  nanoparticles by chemical co-precipitation technique for photo-degradation of organic dye-stuffs under direct sunlight. *Phys. B* **587**, 412136 (2020)
28. G.L. Jadhav, S.D. More, C.M. Kale, K.M. Jadhav, Effect of magnesium substitution on the structural, morphological, optical and wetTableility properties of cobalt ferrite thin films. *Phys. B* **555**, 61–68 (2019)
29. K.R. Babu, R. Singh, Effect of RF power on structural, magnetic, and optical properties of  $\text{CoFe}_2\text{O}_4$  thin films. *J. Supercond. Nov. Magn.* **31**, 4029–4037 (2018)
30. T. Dippong, E.A. Levei, I.G. Deac, E. Neag, O. Cadar, Influence of  $\text{Cu}^{2+}$ ,  $\text{Ni}^{2+}$ , and  $\text{Zn}^{2+}$  ions doping on the structure, morphology, and magnetic properties of Co-Ferrite embedded in  $\text{SiO}_2$  matrix obtained by an innovative sol-gel route. *Nanomaterials* **10**, 580 (2020)
31. K. Dubey, S. Dubey, V. Sahu, R.A. Parry, A. Modi, N.K. Gaur, Structural, optical and magnetic properties of  $\text{CoFe}_2\text{O}_4$  nanoparticle synthesized by ultrasonication–assisted sol–gel technique. *Appl. Phys. A* **128**, 560 (2022)
32. S. Divya, P. Sivaprakash, S. Raja, S.E. Muthu, I. Kim, N. Renuka, S. Arumugam, T.H. Oh, Impact of Zn doping on the dielectric and magnetic properties of  $\text{CoFe}_2\text{O}_4$  nanoparticles. *Ceram. Int.* **48**, 33208–33218 (2022)
33. G.H. Han, M.G. Li, Y.S. Yu, W.W. Yang, J. Li, S.C. Xu, M. Feng, H.B. Li, Structure and magnetic properties of cobalt ferrite foam with low mass density. *J. Alloy Compd.* **790**, 947–954 (2019)
34. A.H.E. Foulani, A. Aamouche, F. Mohseni, J.S. Amaral, D.M. Tobaldi, R.C. Pullar, Effect of surfactants on the optical and magnetic properties of cobalt-zinc ferrite  $\text{Co}_{0.5}\text{Zn}_{0.5}\text{Fe}_2\text{O}_4$ . *J. Alloy Compd.* **774**, 1250–1259 (2018)
35. M. Ounacer, B. Rabi, A. Essoumhi, M. Sajieddine, B.F.O. Costa, M. Emo, A. Razouk, M. Sahlaoui, Influence of  $\text{Al}^{3+}$  substituted cobalt nano-ferrite on structural, morphological and magnetic properties. *J. Alloy Compd.* **854**, 156968 (2020)
36. M.J. Xu, J. Li, Y. Yan, X.G. Zhao, J.F. Yan, Y.H. Zhang, B. Lai, X. Chen, L.P. Song, Catalytic degradation of sulfamethoxazole through peroxymonosulfate activated with expanded graphite loaded  $\text{CoFe}_2\text{O}_4$  particles. *Chem. Eng. J.* **369**, 403–413 (2019)
37. Z.Q. Yang, Y. Li, X.Y. Zhang, X.D. Cui, S. He, H. Liang, A. Ding, Sludge activated carbon-based  $\text{CoFe}_2\text{O}_4$ -SAC nanocomposites used as heterogeneous catalysts for degrading antibiotic norfloxacin through activating peroxymonosulfate. *Chem. Eng. J.* **384**, 123319 (2020)
38. Y.V. Kaneti, Y.N. Guo, N.L.W. Septiani, M. Iqbal, X.C. Jiang, T. Takei, B. Yulianto, Z.A. Alothman, D. Golberg, Y. Yamauchi, Self-templated fabrication of hierarchical hollow Mn-cobalt phosphide yolk-shell spheres for enhanced oxygen evolution reaction. *Chem. Eng. J.* **405**, 126580 (2021)

**Publisher's Note** Springer Nature remains neutral with regard to jurisdictional claims in published maps and institutional affiliations.

Springer Nature or its licensor (e.g. a society or other partner) holds exclusive rights to this article under a publishing agreement with the author(s) or other rightsholder(s); author self-archiving of the accepted manuscript version of this article is solely governed by the terms of such publishing agreement and applicable law.